

# Neural Learning Based Blind Source Separation for Detection of Material Defects in Pulsed Thermography Images

Xin Zhang and Jafar Saniie

*ECASP Research Laboratory (<http://ecasp.ece.iit.edu>)  
Department of Electrical and Computer Engineering  
Illinois Institute of Technology, Chicago, IL, U.S.A.*

Alexander Heifetz

*Nuclear Science and Engineering Division  
Argonne National Laboratory  
Lemont, IL, U.S.A.*

**Abstract**—In this paper, we introduce a neural learning-based approach to blind source separation for detection of material flaws in pulsed thermography (PT) images. This approach can be used to detect internal defects (pores) in metallic Additively Manufactured (AM) materials. Such defects occur in high-strength alloys produced with direct laser sintering AM method for nuclear energy applications. Pulsed thermal imaging system utilizes a high intensity flash lamp to rapidly heat surface of sample, a high sensitivity infrared camera to capture data of surface temperature variations. The data cube obtained with PT (stack of surface temperature images at different times) can be analyzed with image processing algorithms to detect material defects. Compared with conventional nondestructive evaluation (NDE) methods, such as digital radiography and ultrasonic testing, the PT pulsed infrared thermal detection technique has advantages of one-sided non-contact measurements, fast processing of large sample areas captured in one image. Detection of small material defects requires finding features in thermal images, which have signal contrast levels approaching sensitivity limit of IR camera. In this study, an optimized Neural Learning based Blind Source Separation (NLBSS) algorithm, including Principal Component Analysis (PCA), and Independent Component Analysis (ICA) is demonstrated to automatically extract principal temporal and spatial features of thermography frames to enhance flaw detection. By using the NLBSS algorithm, material internal defects can be automatically detected. Furthermore, this processing approach compensates for experimental thermal imaging artifacts, such as noise and uneven heating. By merging artificial intelligence with the photothermic, the NDE system detects internal calibrated defects of various sizes and depths in AM nuclear-grade metallic alloys.

## I. INTRODUCTION

Additive Manufacturing (AM) of metallic components is an emerging method for cost-efficient fabrication for industries such as aerospace and nuclear energy. Recent advances in AM indicate that there are still challenges to wide deployment of AM technology for nuclear reactor construction because of defects introduced into metallic materials during the AM process [1]. AM of high-strength alloys used for nuclear energy applications is currently based on direct laser sintering (DLS) technique. DLS can randomly introduce material flaws consisting of low density regions or pores, which contain non-sintered powder [2].

With the thermal and mechanical material strains in nuclear reactors, a low-density defect can potentially become the seed of a crack [3]. Nondestructive evaluation (NDE) is needed to verify integrity of AM structures before they enter service in a nuclear reactor. Detection of flaws in AM is currently a challenge during manufacturing and post-manufacturing. During manufacturing, application of conventional NDE methods is limited by high temperature of the build, constrained space of the 3D printer chamber, and presence of metallic powder on build surface. Because AM structures typically have complex patterns with discontinuities, and shapes without symmetry of revolution, application of conventional NDE methods, such as ultrasonic tomography and digital radiography is facing challenges as well [4].

Pulsed Thermography (PT) is a promising method for post-manufacturing NDE of AM structures. The method consists of rapidly heating a material surface with a flash, and recording time-resolved thermal images with fast frame infrared camera. Material defects are extracted by analyzing thermal images. Advantages of this method include one-sided non-contact measurements, and fast processing of large sample areas captured in one image. However, detection of fine features in thermal images is affected by image thermal noise patterns [5], uneven heating of the specimen, and edge blurring. Image processing algorithms should be applied to enhance defect detection efficiency. Traditional image processing methods, such as Gaussian filtering, histogram equalization and sharpening can improve defect detection, but each one is limited to solving a single problem. Recently, algorithms such as Pulsed Phase Thermography (PPT) [6] have been proposed to improve thermal imaging quality. The PPT transforms data from time-domain into frequency spectra using one-dimensional Discrete Fourier Transform (DFT) to extract phase features. The PPT method can reduce the effect of uneven heating but is vulnerable to high-frequency noise [6]. A method called Thermographic Signal Reconstruction (TSR) can robustly increase resolution of thermography frames, enhance visibility of defects in temporal and spatial domain [7]. However, TSR algorithm is inefficient since a very large number of frames need to be analyzed.

In this paper, we introduce the Neural Learning based Blind Source Separation (NLBSS) algorithm, which not only

enhances defect detection in time and space, but also automatically separates defects from background and identifies the presence of defects. In NLBSS, we use Principal Component Analysis (PCA) [8] to extract principal features of thermography data, thus reducing thermal imaging noises and artifacts. Next, the Independent Component Analysis (ICA) [9], implemented in a two-layer neural network structure, is applied to automatically separate image regions containing signatures of material defects from image regions which do not contain any material flaws. The neural network structure utilizes the fast fixed-point algorithm for optimization to speed up the defect detection. This approach is computationally simple and requires little memory space. By applying the NLBSS algorithm to experimental thermography data, calibrated subsurface defects of various depths and sizes for the AM metallic material were detected.

## II. METHODOLOGY

### A. Introduction to Pulsed Thermography

In Pulsed Thermography (PT) system shown in Figure 1, a short-duration pulse is emitted by a high intensity flashlight to instantly heat the surface of the specimen. A fast frame infrared camera records images of time-dependent blackbody radiation of material, which gives information about material surface relative temperature transients. Absolute temperature values can be obtained through calibration. After data is acquired by the computer, we deploy image analysis algorithms to analyse images and detect defects.

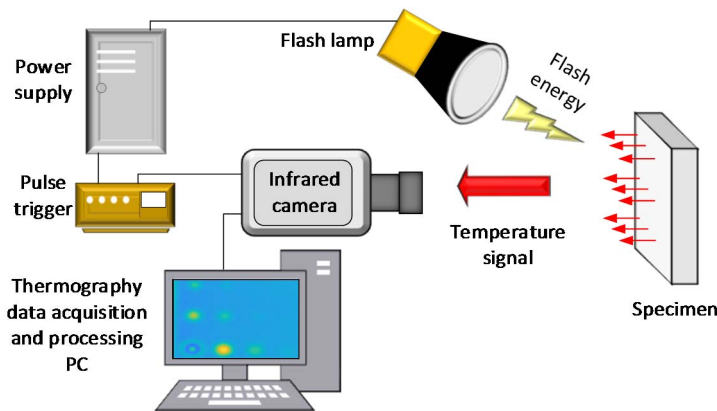


Figure 1. Pulsed Thermography System Design

As shown in Figure 1, the experimental setup includes the IR camera, high-energy flash lamp, power supply, PC, pulse trigger controller, and the specimen. We utilize the Balcar ASYM 6400 power capacitor to deliver a pulse of 6.4 kJ/2ms thermal energy through the flash lamp to heat sample surface. To acquire accurate thermography data, we use FLIR X8501sc IR camera with noise equivalent temperature difference (NETD) of 20mK. During the experiment, we use the trigger controller which is connected to the capacitor, to activate a high-energy flash. The IR camera is synchronized with the flash lamp to start recording the data. The specimen plate is placed with the front side facing the IR camera and the flash lamp.

As heat deposited on material surface starts diffusing into the bulk, surface temperature is rapidly decreasing. Material defects, such as pores containing un-sintered powder, have much lower

thermal diffusivity compared to solid material. Such material defects are acting as thermal resistances which slow down heat diffusion. This leads to appearance of transient “hot spots” on material surface. These are regions on the surface located above material defects, along the direction of heat diffusion. This concept is further elucidated in Figure 2. The red and green curves show temperatures as functions of time for points in surface regions located above defects and not located above defects, respectively. Temperatures of both points rise rapidly at the same rate during the first second as a result of uniform heat deposition on material surface with a flash lamp. After reaching the maximum at approximately  $t=1s$ , both temperatures begin to decay, initially at the same rate. However, after approximately  $t=2s$ , the red curve decays at a much slower rate than the green curve, which gives rise to surface “hot spot.” At a given time, the contrast temperature of the “hot spot” can be obtained from the difference between red and green curves. For example, at  $t=2s$ , the contrast temperature of the “hot spot” is approximately  $3^{\circ}C$ . The “hot spot” is visible between  $t=2s$ , when the diffusing heat front first encounters the material defect, and  $t=7s$ , when material reaches thermal equilibrium. For the temperature values shown in the graphs in Figure 2, the “hot spot” is easily detectable by IR camera with  $NETD=20mK$ . However, for smaller material defects, “hot spot” contrast begins to approach the NETD of a camera. Detection of signals close to camera NETD sensitivity threshold, requires image processing to remove noise and experimental artifacts. Therefore, we apply the NLBSS algorithm to enhance defect detection by the independent source signal separation of defects and non-defects regions for flaws detection.

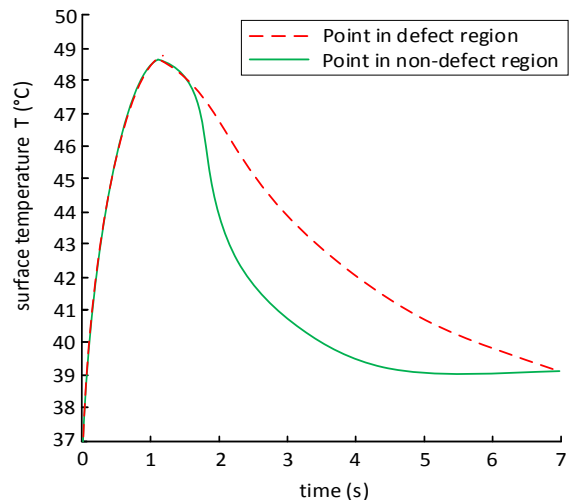


Figure 2. Surface temperature evolution of points in regions above defect (red) and no-defect (green)

### B. Neural Learning based Blind Source Separation

Blind source separation aims at classifying mixed signals into independent source signals without using any a-priori information about the source of signals. In the PT system, the recorded thermography frames (thermograms) are composed of signals from different sources, such as image regions corresponding to defects, regions of no-defects, and noise. Each segment of the thermograms exhibits different temperature evolution during the transient response. In the notation of this

paper, each source signal contributes to the Thermal Source Image (TSI). We utilized the NLBSS algorithm to classify TSI and thus to detect defects. The principle of NLBSS is shown in the flowchart in Figure 3.

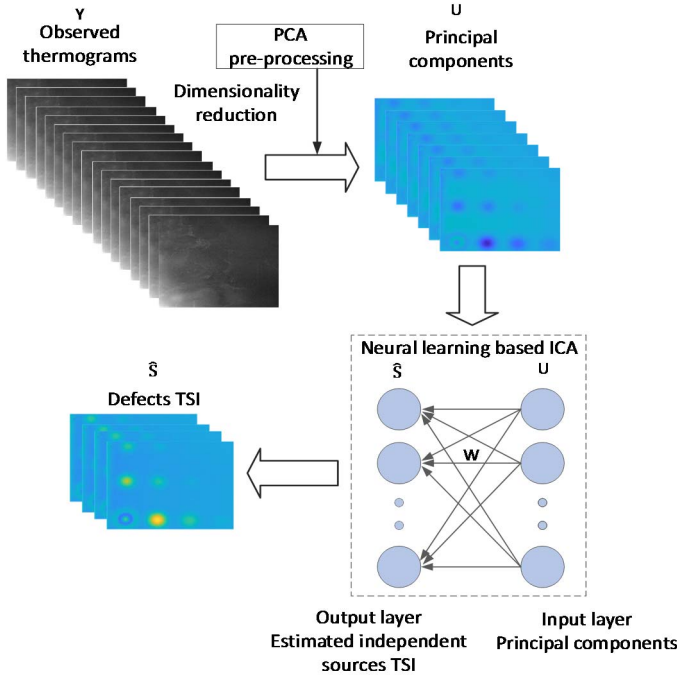


Figure 3. Flowchart of Neural Learning-based Blind Source Separation algorithm

Figure 3 shows the principal processing blocks of NLBSS algorithm. The observed thermograms  $Y$  are mixed with different source signals that need to be separated. As seen in Figure 3, PCA is used to pre-process thermograms  $Y$  to obtain principal components  $U$ . Next, the principal components become inputs to the neural learning-based ICA to estimate independent source signals  $\hat{S}$ , which are TSI's of defects.  $W$  is the estimation matrix for separating the mixed thermograms into TSI's of defects. The neural learning-based ICA is implemented in a neural network structure, which is composed of an input layer and an output layer. The principal components of thermograms  $U$  form the input layer, and each estimated source signal  $\hat{S}$  as a neuron forms the output layer. The input layer and output layer are densely connected.

a) *Principal Component Analysis*: We use the Singular Value Decomposition (SVD) to implement the Principal Component Analysis (PCA). The SVD closely resembles PCA, but suffers less from numerical noise because the covariance matrix does not need to be calculated. The equation implementing SVD is:

$$Y_{M \times N} = U_{M \times N} R_{N \times N} V_{N \times N}^T \quad (1)$$

In order to apply to equation (1) to the thermography data-cube matrix, we transform the total number of pixels in each thermography frame into a single vector to condense the time-dependent information into columns. The condensed 2D data is shown as matrix  $Y$ . In equation (1),  $M, N$  represent the number of rows, columns of matrix  $Y$ , respectively ( $N$  is the number of recorded thermography frames).  $U$  and  $V$  are orthogonal

matrices separately showing variability of data and time information.  $R$  is the matrix containing the singular values of  $Y$ . By decomposing the thermography data  $Y$  with SVD, matrix  $U$  is constructed with PCA basis vectors that describe the largest variability in the data using the first few columns ( $N_f$ ) of  $U$ . These PCA basis vectors are decorrelated to enhance the performance of ICA. Thus, we use only few basis vectors of  $U$ , which contain principal features of data, as input to ICA estimator for detection of flaws.

b) *Independent Component Analysis*: In the PT system, the surface temperature of each image region corresponding to defect ("hot spot") displays the non-Gaussian distribution during transients. However, the distribution of the sum of  $N$  independent source signals approaches Gaussian distribution as  $N \rightarrow \infty$  regardless of the distribution of each signal [9]. Thus, using the mixed thermography data, which is Gaussian, ICA is applied to obtain a separation matrix  $W$  by maximizing the non-Gaussian distribution to detect defects. Equation (2) is used in estimating the TSI of defects  $\hat{S}$  to be as close to the original source signal  $S$  as possible,

$$\hat{S} = WU^T \approx S \quad (2)$$

$$E\{\hat{S}\hat{S}^T\} = I \quad (3)$$

In equation (2),  $U$  is the matrix consisting of principal components of pre-processed thermography data, and  $W$  the separation matrix. In order to achieve high efficiency in defects detection, original source signals need to be statistically uncorrelated and non-Gaussian [9]. Thus, the estimated TSI's of defects are constrained to be uncorrelated under equation (3). Because we apply the PCA to pre-process the thermography data to be uncorrelated in matrix  $U$ , equation (3) is transformed into equation (4) as below:

$$E\{\hat{S}\hat{S}^T\} = WE\{\hat{U}\hat{U}^T\}W^T = WW^T = I \quad (4)$$

In equation (4), the separation matrix  $W$  needs to be orthogonal so that the estimated TSI's of defects  $\hat{S}$  are uncorrelated. Therefore, we applied the neural learning to implement ICA, and use the fast fixed-point algorithm for optimization to obtain  $W$  for defects detection.

The fast fixed-point algorithm is aimed to find a direction to maximize the non-Gaussian properties. In one unit version of this algorithm, to estimate one independent source signal, we need to find a unit vector  $w_i$ , so that the projection  $w_i^T U^T$  maximizes the non-Gaussian. Here  $w_i^T$  is the  $i$ th row vector of matrix  $W$ . Each unit is optimized as a neuron, which is updated with the learning rule. For the multi-unit version of this algorithm, multiple output neurons are built to estimate different source signals. Negentropy [9] is approximated to measure the non-Gaussian:

$$O(w) = [E\{G(w^T U^T)\} - E\{G(g)\}]^2 \quad (5)$$

Equation (5) shows the approximation of negentropy to measure the non-Gaussian as our objective function  $O(w)$ .  $G$  is any nonquadratic function as the contrast function for performance optimization. Here  $g$  is the Gaussian variable with zero mean and unit variance. Then, we use the Newton-Raphson Method [10] to iteratively update the unit vector  $w$  for



maximizing the objective function  $O(w)$  under the constraint given in Equation (4). The specific updates and estimate of  $w$  can be found in [9]. If the convergence is not satisfied, which means that the old and new values of  $w$  still point to different directions, we use the new value of  $w$  to initiate another iteration. Otherwise we apply the direction vector  $w$  to estimate the independent source signal which, is the TSI of defects in the thermal images.

### III. EXPERIMENTAL RESULTS

In order to evaluate the performance of the NLBSS algorithm in detection of flaws, PT images were obtained for AM stainless steel 316 nuclear-grade alloy specimen with calibrated imprinted internal defects [11]. The specimen defects consisted of hemispherical pores with trapped un-sintered powder. Figure 4 shows the photograph of the AM metallic plate (Length  $\times$  Width  $\times$  Thickness: 154 mm  $\times$  72 mm  $\times$  10 mm) manufactured by GPI Industries.



Figure 4. Specimen Plate

The design of embedded calibrated internal defects is shown in Figure 5(a). The labelling scheme in Figure 5(a) is such that, for example, the defect with diameter of 8 mm, located at depth of 5 mm is represented as defect ( $\phi 8, d5$ ). Lower half of the specimen contains larger defects with diameter of 5 mm, 6 mm, 8 mm located at depth of 2 mm, 3 mm, 4 mm and 5 mm. On the upper half of the plate, smaller defects with diameter of 4 mm, 3 mm, 2 mm and 1 mm located at depth of 1 mm, 2 mm, 3 mm, 4 mm and 5 mm are embedded. The depth represents the distance between the defect and the front plate surface, measuring how close the defects are to the surface of the specimen.

To evaluate performance of the NLBSS algorithm, a thermal pattern graph is constructed to show the estimated TSI of defects. In the experiment, surface regions of defects with similar temperature variation are classified as one TSI. Then, the TSI is highlighted to display defects. In the experiment, the specimen is oriented as shown in Figure 5(a). Two separate experiments were conducted. In one, the lower half of the AM plate was imaged to detect larger defects. In another experiment, the upper half of the AM plate was imaged to detect smaller defects. In each experiment, the camera frame resolution was set as  $576 \times 520$  pixels. After thermography frames are acquired by the PC, the NLBSS algorithm is applied to data. We used  $N = 12$  as the number of independent components, which are output neurons, to estimate TSI of defects. The number of principal components was set to  $N_1 = 50$  to reduce noise in the images.

#### A. Detection of Larger Defects

PT imaging was performed on the lower half of the AM plate, as indicated with the red box in Figure 5(a). As shown in Figure 5(a), the defects have diameters of 5 mm, 6 mm, 8 mm, and located at depths of 2 mm, 3 mm, 4 mm and 5 mm. An example of a recorded raw image is shown in Figure 5(b). Results of image processing and defect detection using NLBSS algorithm are shown in Figures 5(c) and 5(d). The defects detected in this experiment are indicated with dashed line ovals in Figure 5(a). In particular, Figure 5(c) clearly shows the defect ( $\phi 8, d2$ ), and Figure 5(d) shows the defect ( $\phi 8, d3$ ), defect ( $\phi 8, d4$ ), defect ( $\phi 6, d2$ ), defect ( $\phi 6, d3$ ), and defect ( $\phi 5, d2$ ). The defect ( $\phi 5, d3$ ), defect ( $\phi 6, d4$ ), and defect ( $\phi 8, d5$ ) are detected with relatively lower confidence.

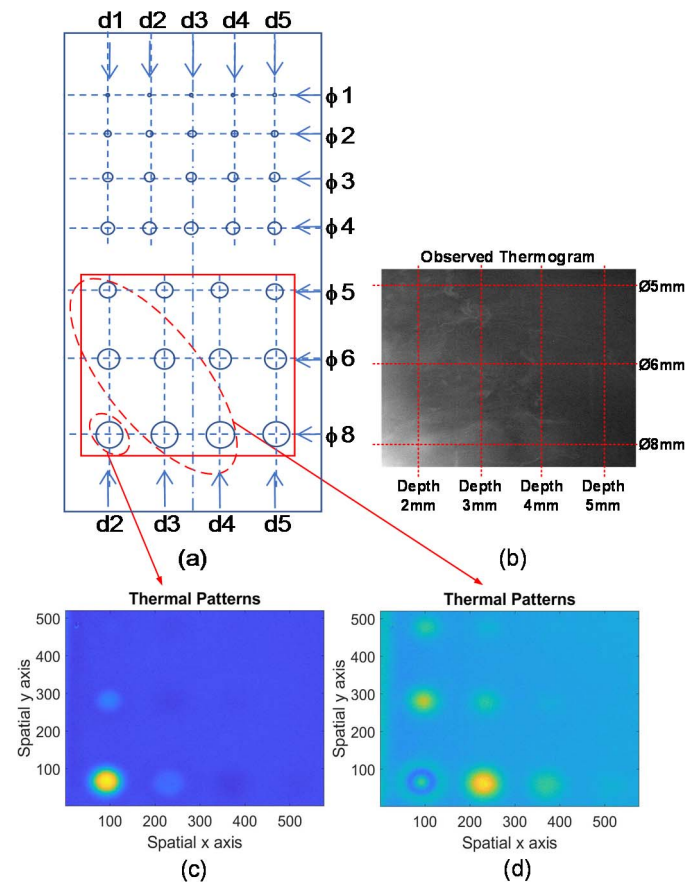


Figure 5. Detection results of larger defects for specimen SSH316

#### B. Detection of Smaller Defects

The experiment was repeated to detect smaller defects in the AM plate. The imaged area of the plate is indicated with a red box in Figure 6(a). Note that Figure 6(a) is Figure 5(a) rotated by 180 degrees. Figure 6(a) shows smaller defects with diameters of 4 mm, 3 mm, 2 mm and 1 mm, and located at depth of 1 mm, 2 mm, 3 mm, 4 mm and 5 mm. Figure 6(b) shows the raw thermogram image recorded with IR camera. After processing the thermograms with the NLBSS algorithm, Figure 6(c) and Figure 6(d) show that the improved detection of defect ( $\phi 4, d1$ ), defect ( $\phi 3, d1$ ), and defect ( $\phi 2, d1$ ), defect ( $\phi 4, d2$ ),

defect ( $\emptyset 3, d2$ ), and defect ( $\emptyset 2, d2$ ). Detected defects are indicated in Figure 6(a) with dashed line ovals.

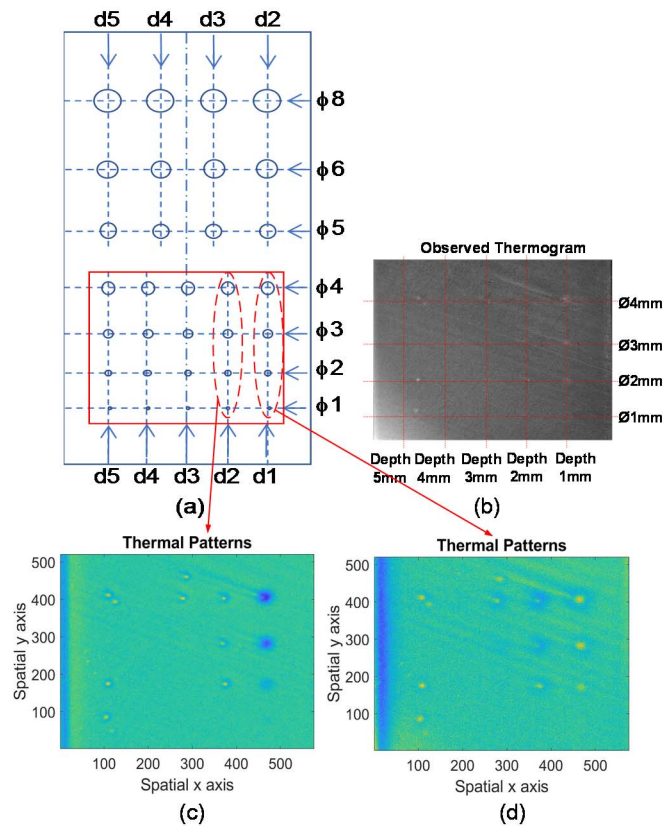


Figure 6. Detection results of smaller defects for specimen SSH316

#### IV. CONCLUSION

In this paper, we developed the Neural Learning-based Blind Source Separation algorithm (NLBSS) to pulsed thermography images to detect internal material defects. We demonstrated application of the NLBSS algorithm to detection of material defects in Additively Manufactured (AM) metals used for nuclear energy applications. The NLBSS algorithm, the Principal Component Analysis (PCA) is applied to pre-process recorded thermograms to enhance defect detection by reducing thermal imaging noise and other experimental artifacts, such as non-uniform illumination of the specimen. Next, Independent Component Analysis (ICA) is used to estimate Thermal Source Images (TSIs) of defects. The ICA is implemented as a two-layer neural network structure, which utilizes the fast fixed-point algorithm for optimization. Our results indicate that internal defects with smaller diameter and deeper location are more difficult to detect. The reason is that defects of smaller size,

located farther from the surface have less effect on reducing the heat diffusion, and thus result in low thermal contrast “hot spots” on the specimen surface. Therefore, to further improve the performance of flaws detection, future work will involve optimizing our NLBSS algorithm, such as deploying advanced neural networks as the hidden layers using the transfer learning, to efficiently extract features of thermograms to enhance defect detection.

#### V. ACKNOWLEDGEMENT

This work was supported in part by the US Department of Energy, Office of Nuclear Energy, Nuclear Energy Enabling Technology (NEET) Advanced Methods of Manufacturing (AMM) program, under contract DE-AC02-06CH11357.

#### REFERENCES

- [1] G. Bertali, Y. Wang, J. Lim, F. Scenini, C. Long, P. Freyer and M. Burke. (2015). “Microstructural Analysis of 3D-Printed Alloy 718,” *Microscopy and Microanalysis*, 21(S3), 463-464.
- [2] A. Heifetz, T.W. Elmer, X. Zhang, J. Saniie. (2019). “PTT System Performance Evaluation in 3-D Imaging of AM Components,” Argonne National Laboratory ANL-19/38.
- [3] M. Wakamatsu, H. Nei and K. Hashiguchi. (1995). “Attenuation of temperature fluctuations in thermal striping,” *J. Nucl. Sci. Technol.*, Volume 32, Issue 8, pp 752-762.
- [4] R. Cunningham, S. P. Narra, C. Montgomery, J. Beuth and A.D. Rollett. (2017). “Synchrotron-based X-ray microtomography characterization of the effect of processing variables on porosity formation in laser power-bed additive manufacturing of Ti-6Al-4V,” Argonne National Lab, *Journal of The Minerals Metals & Materials Society*, Volume 69, Issue3, pp 479-484.
- [5] C. Ibarra-Castaneda, A. Bendada and X. Maldague. (2007). “Thermographic image processing for NDT,” *IV Conferencia Panamericana de END*.
- [6] E. D’Accardi, F. Palano, R. Tamborrino, D. Palumbo, A. Tati, R. Terzi, U. Galietti. (2019). “Pulsed Phase Thermography Approach for the Characterization of Delaminations in CFRP and Comparison to Phased Array Ultrasonic Testing,” *Journal of Nondestructive Evaluation*, Issue 1.
- [7] Steven M. Shepard and Maria Frendberg Beemer. (2015). “Advances in thermographic signal reconstruction,” Proc. SPIE 9485, *Thermosense: Thermal Infrared Applications XXXVII*, Volume: 9485.
- [8] X. Zhang, T. Gonnot, J. Saniie. (2017). “Real-Time Face Detection and Recognition in Complex Background,” *Journal of Signal and Information Processing*, Volume 8.
- [9] A. Hyvärinen. (1999). “The Fixed-Point Algorithm and Maximum Likelihood Estimation for Independent Component Analysis,” *J. Neural Processing Letters*, Volume 10, Issue 1, pp 1-5.
- [10] S. Akram, Q. ul Ann. (2015). “Newton Raphson Method,” *International Journal of Scientific & Engineering Research*, Volume 6, Issue 7.
- [11] A. Heifetz, T. W. Elmer, J. G. Sun, T. Liu, D. Shribak, B. Saboriendo, S. Bakhtiari, X. Zhang, J. Saniie. (2019). “First Annual Report on Pulsed Thermal Tomography Nondestructive Evaluation of Additively Manufactured Reactor Materials and Components: Pulsed Thermal Tomography Nondestructive Examination of Additively Manufactured Reactor Materials and Components,” Argonne National Laboratory ANL-19/43.